Ruddlesden–Popper Sr$_4$Ir$_3$O$_{10}$ perovskite: A new family for water splitting driven by interlayer oxygen migration

Yanhui Sun [a], Yun Hao [a], Jingjun Liu [a,*], Feng Liu [b,*], Jun Gan [b], Shixin Gao [b], Min Liu [c], Lu Liu [c], Wei Zhao [c], Liuli Sun [c], Wu Mei [c], Maorong Chai [c,*]

[a] Beijing Key Laboratory of Electrochemical Process and Technology for Materials, Beijing University of Chemical Technology, Beijing 100029, China
[b] Yunnan Precious Metals Laboratory Co., Ltd., Kunming 650106, China
[c] State Power Investment Corporation Hydrogen Energy Co, Ltd., Beijing 102600 China

ARTICLE INFO

ABSTRACT

Ruddlesden–Popper (R-P) layered perovskites offer a new possibility for efficient water splitting due to their periodically packed rock-salt and perovskite layers along the c-axis in crystallographic. Herein, a novel R-P Sr$_4$Ir$_3$O$_{10}$ oxide with a dynamic characteristic of short-range oxygen migration between the SrO rock-salt monolayer and SrIrO$_3$ perovskite multilayers were fabricated. It shows lower Fermi level around the redox potential level of O$_2$/H$_2$O, which enables an interstitial oxygen assisted lattice oxygen evolution mechanism to improve OER performance with low overpotential of 205 and 278 mV at 10 and 100 mA/cm^2 in acidic environ-ment. In practical proton exchange membrane (PEM) device, the Sr$_4$Ir$_3$O$_{10}$ can sustain more than 50 h without obvious decay at 10 mA/cm^2, steming from a cascade migration of oxygen species from adsorbed water to interstitial oxygen and then lattice oxygen. This may open a new door to developing high-performance R-P perovskites for application in PEM water electrolysis.

1. Introduction

Energy and environmental issues seriously constrain the sustainable development of human society [1–3]. Hydrogen is considered to be the most promising alternative energy carrier in the global energy balance of the future [4–7]. Green hydrogen produced by proton exchange membrane water electrolysis (PEMWE) with renewable electric energy (wind, solar, hydro and so on) has been regarded as one of the most promising carbon-free clean energy (without carbon emission), which contributes to achieve the ambitious goal of carbon neutralization and carbon peak proposed by China in 2060 [8,9]. For PEMWE devices, however, the high overpotential of their anodic oxygen evolution re-action (OER) caused by its intrinsically sluggish kinetics during water splitting lead to an unaffordable power consumption and undesired hydrogen production efficiency in the current PEMWE [10,11]. So, it is still a serious challenge to develop next-generation catalysts with higher activity and stability for OER to replace commercial iridium dioxide (IrO$_2$) that cannot still meet the requirements of long-term industrial water electrolysis to date [12,13].

Ruddlesden–Popper (R-P) perovskites are a promising class of crys-tals with a stoichiometric formula of A$_{n+1}$B$_n$O$_{3n+1}$ (A is alkali metal/ alkaline earth metal, B is transition metal), constructed by periodically packed rock-salt monolayers (AO) and perovskite (ABO$_3$) multilayers along the c-axis in crystallographic [14]. These perovskites show many metric properties, such as stable crystallinity, layered orientation, and perfect phase distribution, which result from a perfectly layered struc-ture. For the rock-salt monolayer existed in R-P perovskites, it features many interstitial oxygen atoms in its tetrahedral interstices. These interstitial oxygen atoms are located near the ($\frac{1}{4}$, $\frac{1}{4}$, $\frac{1}{4}$) sites of the AO orthorhombic Fmmm structure [15,16]. Interestingly, these interstitial

oxygens are unstable and can enter the apical oxygen vacancy of BO_6 octahedron in the ABO_3 perovskite layers via a so-called Frenkel reaction [17]. As a result, these interstitial oxygen atoms have ability to achieve an interesting interlayer migration between the AO and ABO_3 layers to fill the apical oxygen vacancies of BO_6 octahedron. Moreover, after interstitial oxygen atom migration, the generated interstitial oxygen vacancy can also been compensated dynamically by oxygen species from water adsorbed on the rock-salt layer. Diebold et al. [18] have verified that adsorbed water on SrO rock-salt phase can been activated and dissociated easily to form oxygen-based species like OH^-, proved by using low-temperature scanning tunneling microscopy (STM) observation. And then, these OH^- species can efficiently complements the missing interstitial oxygen of SrO monolayer with c-axis expansion, especially under employed anodic potential ranged from 1.2 to 1.9 V condition [19,20]. Such unique oxygen species migration from adsorbed water to interstitial oxygen and lattice oxygen plays a key role in deciding stability of ABO_3 perovskite phase with abundant lattice oxygen vacancy for the R-P oxides.

Recently, there are many published papers have proved that some lattice oxygen in ABO_3-type perovskite directly involved in OER process, proved by in-situ ^{18}O isotope labelling mass spectrometry, in which the lattice oxygen separates from the perovskite crystal to form O_2 to release [21]. The so-called lattice oxygen-evolution mechanism (LOM) has been proposed for OER kinetics, with low free energy barrier for direct O–O coupling. It is much faster than the common adsorption-oxygen evolution mechanism (AEM) in which lattice oxygen not involved but only water as reactant for OER [22–26]. However, the direct involvement of lattice oxygen via LOM to release O_2 can leave many positively charged vacancies in the ABO_3 lattice, resulting in a structural instability [27]. This would lead to serious dissolution of metal cation at B sites or structure collapse, caused by the charge imbalance from lattice oxygen release or stripping in the crystal. This contradiction between catalytic activity and structural stability of perovskites toward OER via LOM has become a frontier scientific challenge hindering the development of high-performance OER catalysts. In our case, the introducing of Ruddlesden–Popper (R-P) perovskites may be a novel strategy to address the above issue, utilizing the interesting cascade migration of oxygen species from adsorbed water to interstitial oxygen and then lattice oxygen for the layered R-P oxides. This way, the stepwise conversion of oxygen can refill the oxygen vacancy in perovskite layers via a hopping mechanism [28], ensuring the structural stability in dynamics during the fast LOM process. Therefore, R-P perovskites with internal oxygen ion migration across layers are a class of promising OER catalysts but has not been reported for application in PEMWE so far.

In this work, we firstly prepared a novel Ruddlesden–Popper perovskite ($Sr_4Ir_3O_{10}$) with a unique characteristic of short-range oxygen migration between the SrO rock-salt layer and $SrIrO_3$ perovskite layers, staring with a sol-gel mixture composed by strontium carbonate, iridium tetrachloride and citric acid, and then followed by solid-phase combustion at high temperature to form the $Sr_4Ir_3O_{10}$ with a layer structure. In acidic environment, the obtained $Sr_4Ir_3O_{10}$ shows a much lower overpotential (205 mV) and far longer stability (35 h) toward OER, compared with a commercial IrO_2. The remarkably improved performance mainly stems from the lowered Fermi level under the redox potential level of O_2/H_2O, which enables LOM pathway over the catalyst. The strong oxygen species conversion from adsorbed water to interstitial oxygen and then lattice oxygen during the OER should be responsible for the long-term durability. This may open a door to developing high-performance R-P perovskites as a class of promising OER electrocatalysts alternative to commercial IrO_2 for application in PEMWE.

2. Experimental section

2.1. Preparation of $Sr_4Ir_3O_{10}$ perovskite

All chemicals are of analytical grade and used without further purification. The water used in all experiments is de-ionized (DI). In a typical preparation procedure of $Sr_4Ir_3O_{10}$ perovskite, 100 mL 10 wt% citric acid solution was prepared and stirred for 30 min, and then 0.004 mol strontium carbonate and 0.002 mol iridium tetrachloride were added to the above solution and stirred for 1 h to form a sol. The obtained sol was evaporated at 90 °C to obtain strontium and iridium mixed gel. After that, putting the dried gel into a muffle furnace to remove citric acid under air atmosphere at 600 °C for 10 h, and then solid-phase heating it at 900 °C for 12 h to obtain the final R-P perovskite $Sr_4Ir_3O_{10}$. For exploring the impact of the feed ratio, the stoichiometric ratio $Sr_4Ir_3O_{10}$ as a reference was also prepared through the same steps, but strontium carbonate and iridium tetrachloride were fed according to the stoichiometric ratio of 4:3.

2.2. Characterization

Scanning electron microscope (SEM) was performed using JEOL-6701 F field emission scanning electron microscope in high-vacuum mode to observe the morphology and size of the catalysts. Transmission electron microscope (TEM) was performed using JSM-2100 high resolution transmission electron microscope for observing the fine microstructure of the sample. X-ray diffractometer (XRD) model RINT2200V/PC was used to characterize the crystal structure, with a Cu target as the radiation source, with a working voltage (40 kV) and current (200 mA). During XRD measurements, the angle range is set to $10° - 90°$ and the scanning rate is $6°/min$. The X-ray photoelectron spectroscopy (XPS) tests were performed with an X-ray photoelectron spectrometer model ESCALAB250 to detect chemical content and valence states of the samples. When processing the XPS data, the C1s spectrum with the center position at 284.6 eV is used for correction to compensate for the surface charge effect. X-band electron paramagnetic resonance (EPR) measurements were performed at room temperature using a Bruker A300–10/12 spectrometer to detect the oxygen vacancy in the perovskite oxides.

2.3. Electrochemical tests

In a standard three-electrode electrochemical system, 0.1 M $HClO_4$ solution was used as the electrolyte, a glassy carbon electrode coated with the catalyst was used as working electrode, with a carbon rod as counter electrode, and a saturated calomel electrode (SCE) as reference electrode. The ink was prepared by mixing 2.5 mg of oxide with 2.5 mg of acidified graphitized carbon black to improve the electrical conductivity. For the working electrode, the total catalyst loading on the glassy carbon electrode is 0.3 mg/cm^2, while the loading of metal Ir is 0.09 mg/cm^2. The tested electrodes are activated by using cyclic voltammetry (CV) at a scanning rate of 100 mV/s for 20 cycles with a potential range of 0.8–1.1 V relative to SCE. The iR-compensation linear sweep voltammogram (LSV) tests were conducted at a scanning speed of 50 mV/s with the potential range of 0.7–1.4 V relative to SCE. The constant current test was conducted at a constant current density of 10 mA/cm^2 to evaluate stability of the catalysts for OER.

The $Sr_4Ir_3O_{10}/IrO_2$ and commercial Pt/C were used as anode and cathode catalyst to assemble a PEMWE device, which was composed of titanium electrode plate, titanium felt collector and Membrane electrode assemblies (MEAs). MEAs were manufactured using the catalyst coated membrane (CCM) method and the $Sr_4Ir_3O_{10}$ served as anodic catalyst and commercial Pt/C (20% Pt) as cathodic catalyst were sprayed respectively onto N117 membrane to form MEA with a working area of 1.5×1.5 cm^2, aiming to avoid the impact of complexity of device on test results. The loadings of the catalysts on the anode and cathode were
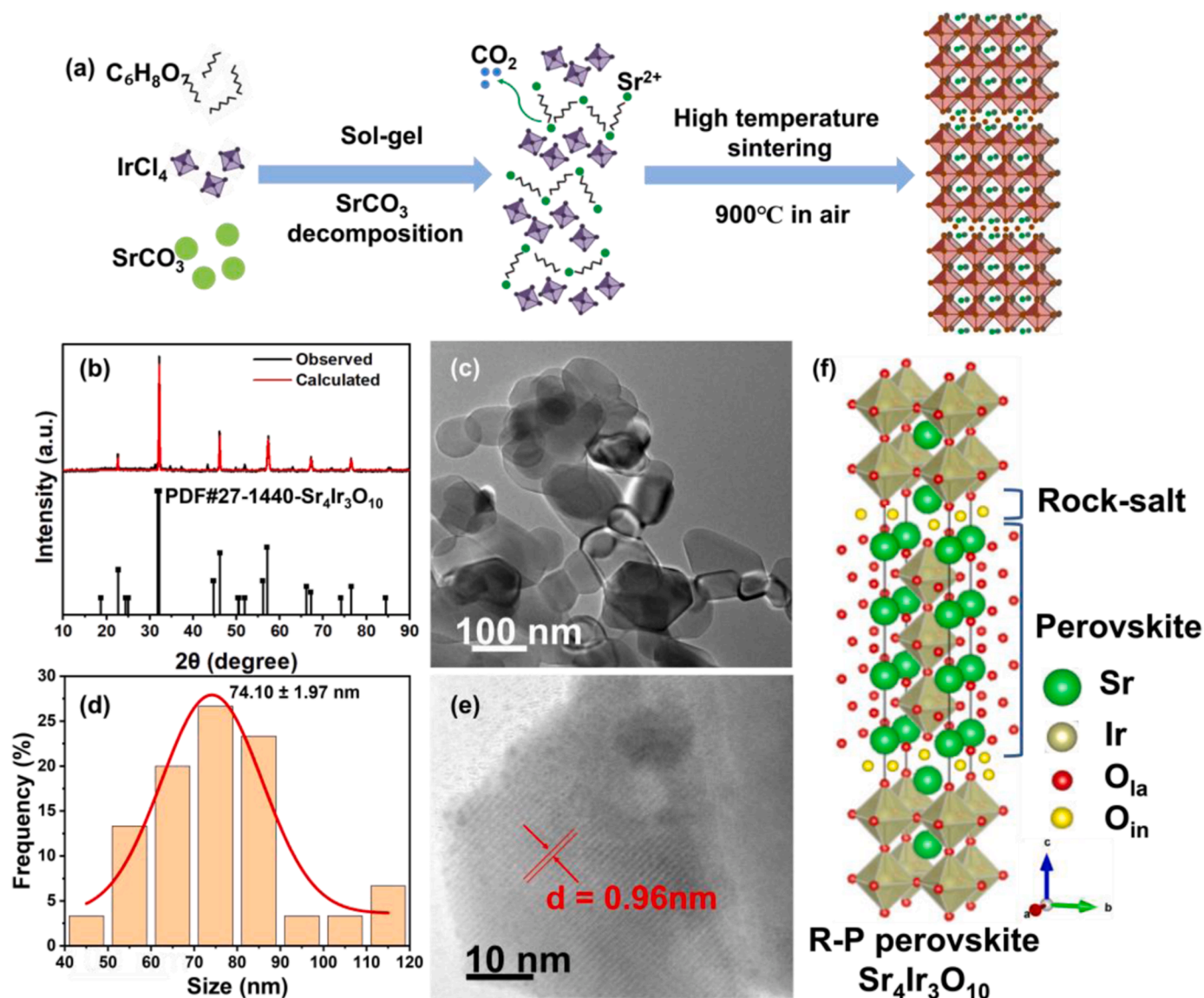
Fig. 1. (a) Schematic synthesis diagram of $Sr_4Ir_3O_{10}$. (b) XRD pattern. (c) TEM image. (d) Size distribution. (e) HR-TEM images. (f) Crystal structure of the above $Sr_4Ir_3O_{10}$.

$0.3 \ mg.cm^{-2}$, respectively. To accurately evaluate the performance of catalysts and avoid the influence of electrolyte conductivity, 0.1 M $HClO_4$ aqueous solution is supplied by the peristaltic pump, and the given flow at the anode is 100 mL/min. The polarization curves were collected at a cell voltage range from 1.0 to 1.8 V at 50 °C, with a scanning rate of 10 mV/s. The stability of PEMWE was evaluated by the constant current test under the constant current density of 10 mA/cm^2.

2.4. DFT calculation

DFT simulations were performed with the DMol3 module of Materials Studio (MS). The generalized gradient approximation (GGA) of Perdew-Burke-Ernzerhof (PBE) functional and the projector augmented-wave (PAW) potential were employed [29]. The layered $Sr_4Ir_3O_{10}$ perovskite with SrO monolayer terminated surface was selected as our pristine slab model, and 4×4 supercell was established. The periodic boundary condition (PBC) was set with a 20 Å vacuum region above surface to avoid the attractions from adjacent periodic mirror images. An energy cutoff of 500 eV was used for the plane-wave expansion of the electronic wave function for all numerical calculations with a Monkhorst-Pack mesh of $3 \times 3 \times 1$. The convergence criterion of force

and energy were set to be $10^{-2} \ eV/Å$ and 10^{-5} eV, respectively. The relative location of various atoms was determined by the slab model with the lowest energy. The solvation-correction slab model is realized by introducing a hybrid solvation model, in which the implicit solvation model is applied by using DMol3 solvent with a dielectric constant of 78.54 for water solvent and the explicit model has also been used to mimic the solvent−intermediate interactions.

The computational hydrogen electrode (CHE) model [30] was applied to simulate the OER pathway and determine the reaction energy barrier for different slab models. Various oxygen species intermediates were considered and the related adsorption energy (ΔE_{ads}) of those intermediates were calculated according to Eq. (1) [31]:

$$\Delta E_{ads} = E_{total} - E_{sub} - E_{ads} \tag{1}$$

where E_{total}, E_{sub}, and E_{ads} represent the total energies determined by the system, the substrate, and the adsorbate, respectively. The Gibbs free energy change (ΔG) of each step in OER is defined as Eq. (2) [31]:

$$\Delta G = \Delta E + \Delta ZPE - T\Delta S \tag{2}$$

where ΔE is the electronic energy difference, ΔZPE and ΔS are the

difference of zero-point energies and the change of entropy, respectively, which is estimated from the vibrational frequencies, and T = 298.15 K.

The interaction between water layer and oxide surface is a cumulative effect of both water−water and oxide−water interactions. Hence, to decouple these interactions, we have calculated the hydrogen bonding energy in the water layer as Eq. (3) [32]:

$$E_{HB} = [E_{H2O}(monomer) \times N - E_{H2O}(WL)] / N \qquad (3)$$

where E_{HB} is the energy of hydrogen bond between water layer and attributed to the water−water interactions; E_{H2O} (monomer) is the total

energy of the water monomer on the surface; N is the number of water molecules in the unit cell, and E_{H2O} (WL) is the energy of the water layer in the optimized geometry of the oxide-water system. The average adsorption energies of the water bilayers are calculated as Eq. (4) [34]:

$$E_{ads} = [E_{H2O}(monomer) \times N + E_{oxide}] - E_{oxide-water} / N \qquad (4)$$

where E_{ads} is the energy of adsorption energy of water on the oxide surface, assigning the oxide−water interactions; E_{oxide} is the total energy of the bare surface, $E_{oxide-water}$ is the total energy of the water layer adsorbed surface system.
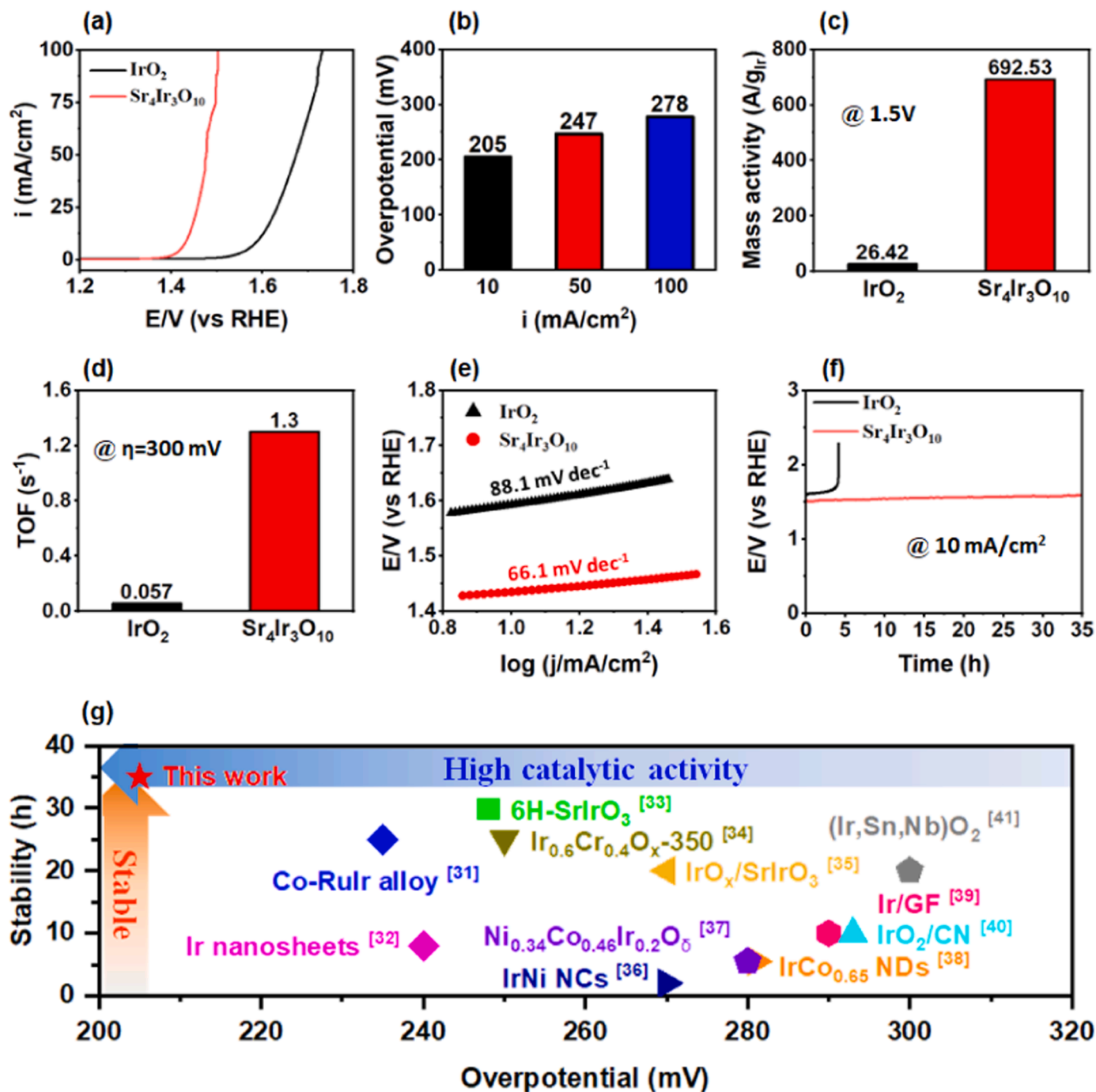
Fig. 2. (a) OER polarization curves of $Sr_4Ir_3O_{10}$ and commercial IrO_2 in 0.1 M $HClO_4$. (b) Overpotentials of $Sr_4Ir_3O_{10}$ (recorded at 10, 50 and 100 mA/cm^2, respectively). (c) MA at 1.5 V (normalization by the mass of Ir). (d) TOF for the $Sr_4Ir_3O_{10}$ and IrO_2. (e) Tafel slopes. (f) Electrochemical stability of $Sr_4Ir_3O_{10}$ and IrO_2 by chronopotentiometry at 10 mA/cm^2. (g) Comparison of the activity and stability of this catalyst with previously reported Ir-based catalysts.

3. Results and discussion

3.1. Fabrication of layered R-P $Sr_4Ir_3O_{10}$ perovskite

Fig. 1a shows a typical fabrication procedure of the target R-P $Sr_4Ir_3O_{10}$ perovskites with a unique layered structure constructed by SrO rock-salt monolayer and three $SrIrO_3$ perovskite layers, staring with a sol-gel precursor containing strontium carbonate, iridium tetrachloride and citric acid, and then following solid-phase combustion and sintering at high temperature to form a perovskite oxide. During the sol-gel stage, the added strontium carbonate can react with citric acid to release CO_2, leaving Sr^{2+} ions coordinated with citrate anion in the sol. A strong stirring effect produced by the released CO_2 makes the $Sr^{2+}/$ citrate complexes fully mixed with the iridium salt to form a highly dispersed sol shown in Fig. S1. After water evaporation, the obtained gel remains a molecular equidistribution of iridium tetrachloride complexed and dispersed by strontium citrate via an electrostatic repulsion. A homogeneous solid-phase power and no impurity phases can be observed for the dried gel shown in Fig. S2. And then, a solid-phase combustion and sintering were performed for the above gel at 900 ℃ in air to fully remove citric acid, enabling the released Sr^{2+} ions diffuse into the vacancies enclosed by the IrO_6 octahedron to form a $SrIrO_3$ perovskite component. At the same time, some Sr^{2+} species combine with oxygen from air, forming SrO monolayer covered on the $SrIrO_3$ surface to reduce the free energy of the oxide [33]. The residual Sr^{2+} in form of unstable strontium citrate is fully removed through a solid-phase volatilization at this combustion and sintering temperature (>600 ℃). This formation process of the $Sr_4Ir_3O_{10}$ illustrates that the adding excessive strontium salt is one of the key roles in the controllable synthesis of the oxide with a stoichiometry. In view of thermodynamic mechanism, the formation process of the oxides with SrO rock-salt layer-covered $SrIrO_3$ perovskite is dynamically spontaneous at high temperature, since the atom radius (R) ratio of two metals like Sr and Ir meets the reported formula of 1.6 $R_{Ir} < R_{Sr} < 1.24 R_{Ir} + 0.9$ Å [14]. As evidenced by XRD results shown in Fig. 1b, all the diffraction peaks of the obtained oxide match well with the corresponding ones (JCPDS No.27–1440) for R-P $Sr_4Ir_3O_{10}$ perovskite and no impurity phases like Sr- or Ir- oxides were observed here. The fitted XRD results in Fig. 1b provides another evidence for the formation of the pure R-P $Sr_4Ir_3O_{10}$ with a space group is I4/mmm [34]. And also, the additional XPS data only detect Sr, Ir and O species without Cl peak, revealing the synthesized R-P $Sr_4Ir_3O_{10}$ having no iridium chloride residue shown in Fig. S3. Additional ICP-OES/MS tests were performed to further determine the contents of Sr and Ir in the R-P $Sr_4Ir_3O_{10}$ shown in Table S1. The Ir percent is 20.74 at% and the Sr percent is 27.52 at%, relative to total oxide. The atomic ratio of Sr and Ir is about 4:3 in the $Sr_4Ir_3O_{10}$, which is lower than the atomic ratio of Sr and Ir determined by XPS analysis (Fig. S3). The relatively high Sr content on the surface is due to the presence of SrO rock salt layer on the catalyst surface.

The typical morphology of the as-prepared $Sr_4Ir_3O_{10}$ is shown in Fig. 1c. It presents an irregular and granular shape in nanoscale and the nanoparticle distribution is relatively uniform and no obvious agglomeration were observed from Fig. S4. From Fig. 1d, the average size of the $Sr_4Ir_3O_{10}$ nanoparticles is around 74.10 ± 1.97 nm, similar to the result calculated by Scherrer formula from XRD (67.23 nm) in Table S2. The high-resolution TEM images show a clear crystalline lattice fringe (0.96 nm) in Fig. 1e, which corresponds to 3 perovskite blocks separated by SrO rock-salt layers [35]. It offers a direct prove for the formation of the layered R-P $Sr_4Ir_3O_{10}$ perovskite via the proposed stepwise two-step method above. Based on the lattice parameters of $Sr_4Ir_3O_{10}$ perovskite with a layered structure, the optimized atomistic structure of the oxide is shown in Fig. 1f. The structural model is periodically built by three $SrIrO_3$ perovskite layers and SrO rock-salt monolayer to form a typical R-P $Sr_4Ir_3O_{10}$ perovskite structure. It is believed that the $Sr_4Ir_3O_{10}$ is a typical R-P perovskite with layered structure, as evidenced by published papers [36]. In a unit cell of the perovskite, two groups of triple IrO_6

octahedra arrange along the crystallographic c axis. $Sr_4Ir_3O_{10}$ was reported to be a tetragonal structure (a=b=3.99 Å, c=28.78 Å. $\alpha = \beta = \gamma = 90°$) with space group I4/mmm (No. 139). As a result, all the oxygen atoms in the layered perovskite can been divided two categories. One is majority lattice oxygen located at the vertex of IrO_6 octahedron (O_{la}) while the other is minority interstitial oxygen (O_{in}) existed in the tetrahedral interstice of SrO monolayer shown in Fig. 1f. The O_{in} species may come from air because oxygen in air can enter easily into the interstices of SrO monolayers to become interstitial oxygen [37], which contributes to remarkably increase structural stability of the layered oxides. More importantly, the heterogeneous layered structure of the $Sr_4Ir_3O_{10}$, constructed by SrO rock-salt monolayer and $SrIrO_3$ perovskite multilayers, may lead to a certain internal strain by particle-induced structural distortion. This conjecture can be confirmed by an obvious shift of the large angle peak at 2θ= 76.52° in the tested signals relative to JCPDS No.27–1440 shown in Fig. 1b. The internal strain is up to 0.33% shown in Fig. S5, determined by the data from the fitted XRD results in Fig. 1b. For the layered oxide, the strain can either activate Ir atoms via a Ir redox chemistry (with the metal bands around the Fermi level) or activate lattice oxygen atoms via an oxygen redox chemistry (with oxygen bands around the Fermi level), which contribute to OER process over the oxide [38].

To give insight into the effect of excessive strontium salt on the morphology and structure of the oxides, we carried out a control experiment with a lower strontium salt feed under the similar synthesis condition shown in Fig. 1a. As the added feed of strontium carbonate decreases to a theoretical stoichiometric ratio of Sr and Ir (Sr: Ir = 4:3), the obtained products are still the pure $Sr_4Ir_3O_{10}$ perovskite evidenced by the XRD results in Fig. S6. However, the obtained oxide become larger in size (Fig. S7), compared with the sample fabricated at Sr: Ir= 2:1 shown in Fig. S4. It further verifies that the excess of strontium carbonate feed above the stoichiometric ratio is the key to obtain a smaller $Sr_4Ir_3O_{10}$ oxide, through a stirring mechanism of strontium compound volatilization or sublimation. The smaller particle size of the oxide results in a larger electrochemical specific surface area, which facilitates the OER rate.

3.2. High performance toward OER

The OER performance of the as-synthesized layered R-P $Sr_4Ir_3O_{10}$ perovskite fabricated at a feed atomic ratio (Sr: Ir=2:1) were firstly benchmarked in an acid electrolyte and the collected linear sweep voltammogram (LSV) curves are shown in Fig. 2a. As observed, the catalyst shows a much better OER activity than that obtained by a commercial IrO_2 as reference or by a control $Sr_4Ir_3O_{10}$ with a larger size (fabricated at the stoichiometric Sr: Ir=4:3) shown in Fig. S8. An potential of 1.435 V is required for the smaller $Sr_4Ir_3O_{10}$ at a current density of 10 mA/cm² (normalized by geometrical area of electrode) while the potential of 1.593 V for the commercial IrO_2, showing it significantly outperform the commercial the-state-of-art IrO_2. With increasing current density, the $Sr_4Ir_3O_{10}$ only requires the potentials of 1.477 and 1.508 V to reach the current densities of 50 and 100 mA/cm² respectively. From Fig. 2b, at given different polarization current densities (10, 50, 100 mA/cm²), the recorded overpotentials for the catalyst are 205, 247, 278 mV respectively, which are significantly lower than those by IrO_2 (363, 443, 502 mV). In order to predict the catalytic ability of $Sr_4Ir_3O_{10}$ at higher current densities, we fitted the current-overpotential curve according to the measured data. According to the fitting curves shown in Fig. S9 and Fig. S10, the trend in the overpotential for the $Sr_4Ir_3O_{10}$ is obviously lower than that of the IrO_2. It is predicted that the $Sr_4Ir_3O_{10}$ can reach a large current density of 1 A/cm² with a potential of 1.63 V, while IrO_2 needs 1.99 V, indicating that the synthesized catalyst has better catalytic ability, which is more in line with the industrial needs of water splitting.

To explore the intrinsic activity toward OER, the mass activity (MA) of the catalysts, normalized by Ir loading on the working electrode, was
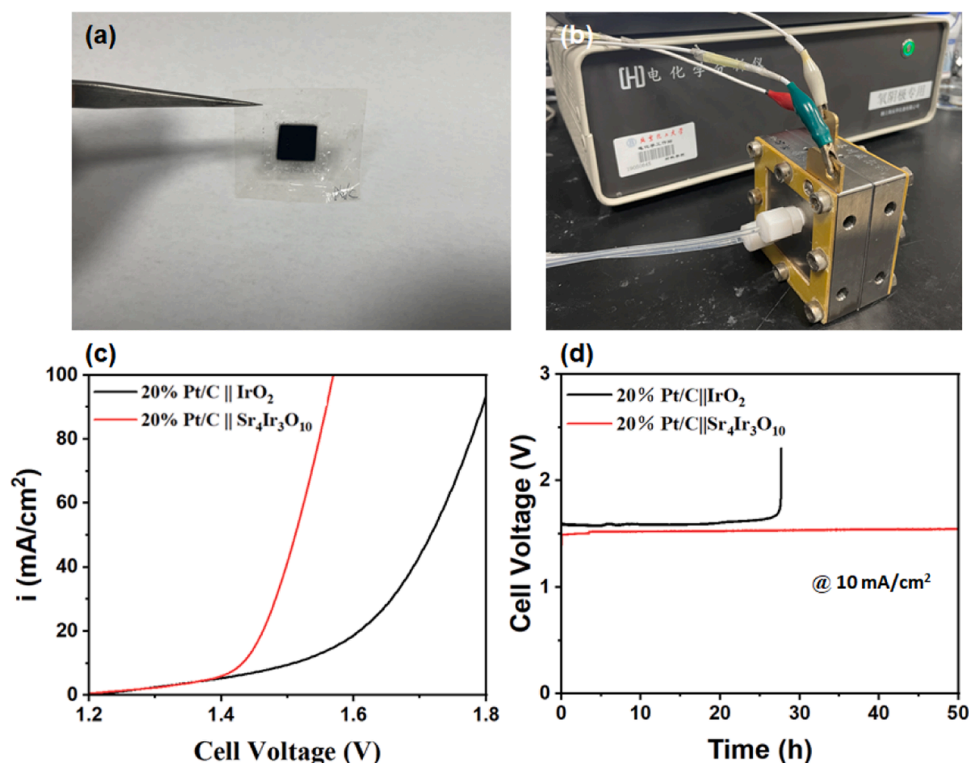
Fig. 3. (a) Actual image of the as-prepared CCM. (b) Actual image of the electrolyzer during the test. (c) Cell voltage–current density curve. (e) The typical galvanostatic curves of the as-assembled PEM electrolyzer ($Sr_4Ir_3O_{10}$ as the anode and Pt/C as the cathode) at 10 mA/cm^2.

determined and the obtained outcomes are shown in Fig. 2c. The $Sr_4Ir_3O_{10}$ delivers a high mass activity of 692.53 A/g$_{Ir}$ at a potential of 1.5 V, while only 26.42 A/g$_{Ir}$ are observed for IrO_2, respectively (Fig. 2c). A similar tendency can also be observed for Turnover frequency (TOFs) in Fig. 2d. The recorded TOF of the catalyst reaches 1.3 s^{-1} at an overpotential of 300 mV, 22.8 times higher than that of IrO_2. The obvious increased intrinsic activity indicates that the active sites in the layered R-P perovskite feature a much greater contribution to OER kinetics than that in IrO_2. To further probe reaction kinetics, the Tafel plots were determined and corresponding results are shown in Fig. 2e. As depicted, the recorded Tafel slope is 66.1 mV/dec for the $Sr_4Ir_3O_{10}$ whereas 88.1 mV/dec for IrO_2, which has considerably reduced by 22 mV/dec. It implies an accelerated OER kinetics in water splitting via unique lattice and/or interstitial oxygen activation mechanism for the $Sr_4Ir_3O_{10}$ catalyst. More importantly, the catalyst also exhibits very good long-term stability, as evidenced by the chronoamperometric (CP) results shown in Fig. 2f. As observed, after 35 h continuous CP measurements, the OER activity of the catalyst remains almost unchangeable, whereas IrO_2 catalyst rapidly deactivates within 5 h, noted that the synthesized $Sr_4Ir_3O_{10}$ has not only superior OER activity, but also outstanding electrocatalytic stability, compared with the common IrO_2 catalyst. Moreover, from the graphical results in Fig. 2g, it is noted that the layered R-P $Sr_4Ir_3O_{10}$ perovskite is superior to the current the-state-of-art Ir-based catalysts from two aspects of activity and stability toward OER during acidic water splitting. [39–49].

Moreover, the novel $Sr_4Ir_3O_{10}$ was employed as anodic catalyst and 20 wt% Pt/C as cathodic catalyst coated onto a commercial N117 proton exchange membrane to prepare a home-made MEA (Fig. 3a), and then MEA-equipped PEMWE device is shown in Fig. 3b. As a result, at a given 50 mA/cm^2, the recorded cell voltage of the $Sr_4Ir_3O_{10}$-Pt/C PEMWE is about 1.47 V, much lower than that obtained by IrO_2 (1.725 V), as evidenced by the results in Fig. 3c. The recorded device performance is comparable to the best OER electrocatalyst recently reported [50,51], although our PEMWE device operating under lower temperature

conditions (50 ℃). Additionally, we also evaluated the long-term stability of PEMWE device and the obtained results are shown in Fig. 3(d). The $Sr_4Ir_3O_{10}$ and IrO_2 loadings on the anode are 0.3 mg.cm^{-2} (not normalized to Ir content), respectively. IrO_2-equipped device shows a distinct voltage change and become inactive in less than 30 h. However, the $Sr_4Ir_3O_{10}$-equipped PEMWE device shows remarkable durability, operating stably for more than 50 h without obvious decaying cell voltage under the same test conditions. These outcomes provide another prove for promising application of the novel $Sr_4Ir_3O_{10}$ catalyst for green hydrogen production in industry.

After 50 h stability test in PEMWE device, the spent $Sr_4Ir_3O_{10}$ catalysts were collected and post-characterized. The morphology and structure of the spent catalyst match those of the fresh one very well, based on the TEM and XRD results before and after the stability test, as shown in Fig. 1b-c and Fig. S11a- b. The average size of the catalyst nanoparticles after the stability tests is around 73.28 ± 1.65 nm, similar to that of initial one. After OER running, Ir atoms in the $Sr_4Ir_3O_{10}$ still mainly exists in the form of minority tetravalent and majority pentavalent (Fig. S11c) and the obtained Sr 3d spectrum similar to that of the fresh catalyst (Fig. S11d). Moreover, there are no obvious peak shifts observing in Sr 3d and Ir 4 f spectra after stability test, which suggested $Sr_4Ir_3O_{10}$ possessed outstanding stability.

3.3. Activation and stabilization driven by interlayer oxygen migration

According to the unique layered structure of the as-synthesized R-P $Sr_4Ir_3O_{10}$ perovskite shown in Fig. 1f, the exact mechanism for OER over it has been identified in acidic electrolyte, as shown in Fig. 4. From the basic kinetics of OER, there are two mainstream mechanisms categorized as: (1) One is an adsorption-oxygen evolution mechanism (AEM) in which the adsorbed water molecules/hydroxyl species participate in the OER to release O_2 and (2) Another is a lattice oxygen-evolution mechanism (LOM) in which lattice oxygen participates in the oxygen evolution and leaves some lattice oxygen vacancies for the catalysts [39]. On
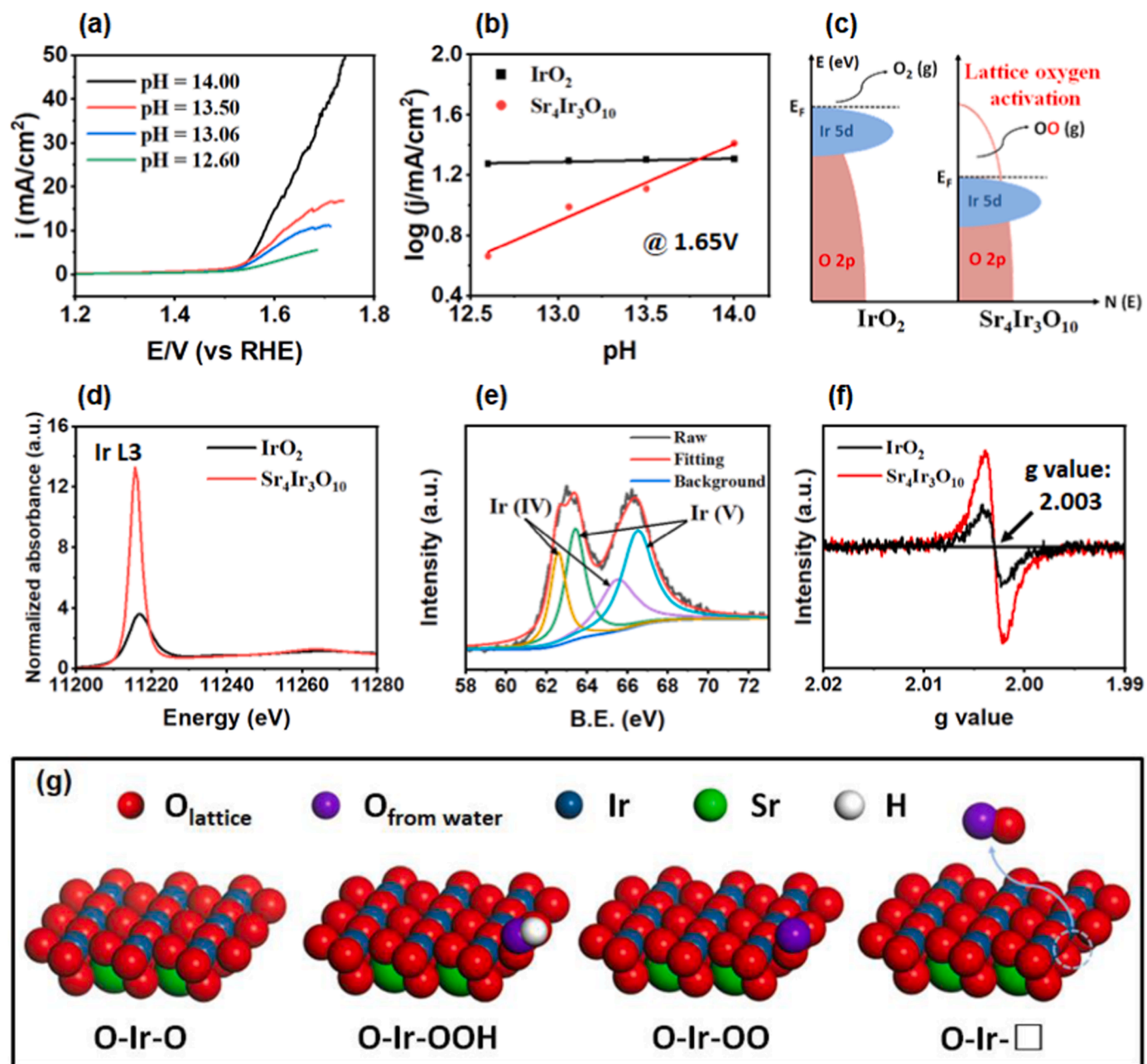
Fig. 4. (a) pH dependence of OER activities of $Sr_4Ir_3O_{10}$. (b) Current densities at 1.65 V versus RHE as a function of pH value for $Sr_4Ir_3O_{10}$ and IrO_2. (c) Energy bands. (d) L3-edge normalized XANES spectra. (e) Ir 4 f XPS spectra. (f) EPR curves of $Sr_4Ir_3O_{10}$ and IrO_2. (g) Schematic of LOM process.

an electrochemical catalyst, the overall reaction usually consists of a series of elementary processes: adsorption/desorption, bond breaking and reorganization, and electron transfer. Though electron transfer and bond cleavage steps typically are rate limiting, adsorption strength and conformation play a critical role in defining the dominant reaction pathway. [52] In our case, the novel $Sr_4Ir_3O_{10}$ seems to trigger the LOM that is faster than the AEM, because of the substantially improved OER activity shown in Fig. 2a. To further confirm this, we measured a set of LSV curves at different pH to determine the LOM pathway that is a proton sensitive by coupling the electron transfer during OER [53]. As shown in Fig. 4a, in an alkaline environment with different pH, the recorded OER activity increases along with increasing pH, indicating a proton-sensitive OER process to follow LOM pathway. Such LOM pathway can avoid the committed step from O* intermediate with high energy barrier to OOH* intermediate existed in the AEM, thus exhibiting a faster OER kinetics. From Fig. 4b, the reaction order of OER over the

$Sr_4Ir_3O_{10}$ catalyst, determined by the slope of the fitting line between the logarithm of current density and proton concentration (pH) is 0.512, which is higher than that obtained by AEM pathway [54]. It provides another evidence for the OER process on the catalyst via a faster LOM pathway. For comparison, IrO_2 display a pH-independent and slow OER activity with reaction order of about 0, as shown in Fig. 4b and Fig. S12. The sluggish OER is attributed to a Fermi energy level of IrO_2 band is much higher than the standard potential of oxygen precipitation (usually 1.23 V) shown in Fig. 4c. Different from IrO_2, the novel $Sr_4Ir_3O_{10}$ features a strengthened Ir-O bond through coupling between Ir 5d orbital and O 2p orbital, caused by the internal strain within the distorted layered structure constructed by SrO rock-salt monolayer and $SrIrO_3$ multilayers shown in Fig. 1b and Fig. S5. As the Ir-O bond is strengthened, the d orbitals of the Ir ion have a greater overlap with p orbitals of the O^{2-} ion, leading to the formation of π * and σ * bands, when the overlap is great enough, ligand holes (oxygen vacancies) are
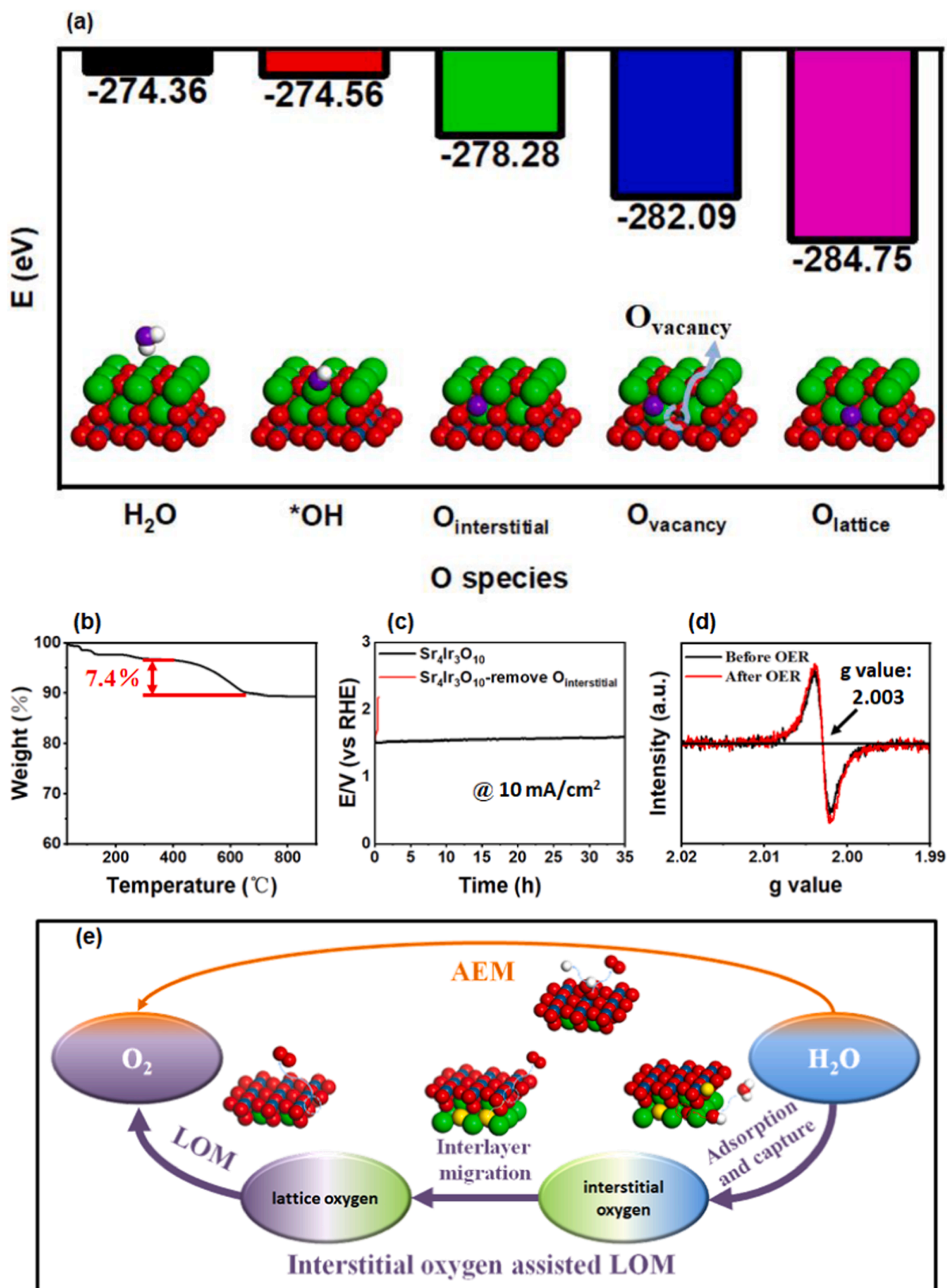
Fig. 5. (a) Energies of different oxygen species. (b) H_2 thermogravimetric curve. (c) Stability before and after interstitial oxygen removal. (d) EPR curves before and after stability tests. (e) Schematic diagram of closed-loop water splitting over $Sr_4Ir_3O_{10}$.

formed and the metal 5d π^* band can no longer be treated as isolated in energy from the oxygen O 2p π^* band [55]. In this way, direct O-O coupling on O 2p states above the Fermi energy level will be thermodynamically favored, O 2p can be activated as the redox active center of the electrochemical reaction and lead to the LOM mechanism [56]. As the Fermi energy level drops around 1.23 V, the lattice oxygen (with bands above 1.23 V) will be activated to easily participate in OER process via LOM pathway. Therefore, the strain can activate the oxide (with the band around the Fermi level) via Ir and lattice oxygen redox chemistry, which drives OER process.

To explore the energy band or Fermi energy level of the strained $Sr_4Ir_3O_{10}$, we calculated the PDOS of the Ir 5d and O 2p orbits for the tested sample and IrO_2 as reference, and the obtained results are shown in Fig. S13-S16. For the tested $Sr_4Ir_3O_{10}$ relative to IrO_2, the recorded Ir 5d D-band center is lower while the p-band center of O 2p is higher shown in Fig. S17 and Fig. S18. The shifted energy bands reveal that the synthesized $Sr_4Ir_3O_{10}$ is conducive to better Ir-O coupling to activate lattice oxygen and has more activated lattice oxygen to participate in the LOM process via a reduced Fermi energy level, as shown in Fig. 4c. To further confirm the reduced Fermi level, synchrotron radiation measurements were performed for the as-synthesized $Sr_4Ir_3O_{10}$, combined with the other characterizations like XPS and EPR. As observed in Fig. 4d, the white line intensity of Ir atoms in the $Sr_4Ir_3O_{10}$ is obviously higher than that of IrO_2, revealing that the valence state of the Ir in the perovskite is much higher than that of IrO_2. This overoxidation of Ir could lead to a decline of 5d orbit, so that the metal can be better coupled with the O 2p orbit with a lower Fermi energy level [57]. From XPS Ir peak splitting results shown in Fig. 4e, the Ir over-oxidative Ir atoms in the $Sr_4Ir_3O_{10}$ mainly exists in the form of minority tetravalent and majority pentavalent, while the Ir in IrO_2 is in the form of zero and tetravalent respectively (Fig. S19). As evidenced by XAFS results in Fig. S20 and Fig. S21, the distance between Ir-Ir bonds in the $Sr_4Ir_3O_{10}$ is shorter than that obtained by IrO_2. The shortened Ir-Ir bonds, caused by the internal strain in the layered structure, contribute to the Coulomb force between Ir-O [58] as a result of the overoxidation of Ir atoms in the oxide. It has been proved that the overoxidation of Ir can activate the adjacent lattice oxygen to trigger LOM pathway in OER [25]. Moreover, the occurred LOM process can be verified further by the EPR test results, as shown in Fig. 4 f. As observed, the signal intensity of lattice oxygen vacancies for the $Sr_4Ir_3O_{10}$ is significantly higher than that of IrO_2, which contribute to OER kinetics via LOM pathway. In addition, the additional XPS results in Fig. S22 and Fig. S23 also prove that the $Sr_4Ir_3O_{10}$ has abundant oxygen vacancies with respect to IrO_2, which could supply the active sites for adsorption and activation of reactants [59]. There is an obvious oxygen vacancy satellite peak in $Sr_4Ir_3O_{10}$, but no oxygen vacancy signal is detected in IrO_2. Therefore, the outstanding OER activity should be responsible for the occurrence of the fast LOM mechanism in OER, further trigged by the strain in the as-synthesized $Sr_4Ir_3O_{10}$ with a layered structure. Fig. 4 g shows the atom-level LOM process over the $Sr_4Ir_3O_{10}$ for OER, where some lattice oxygen at the surface of the perovskite layer can combine with adsorbed oxygen from solvent water molecules and then release oxygen molecules in acidic environment.

The desired LOM process is fast in kinetics but it may leave lattice oxygen vacancies left by O_2, which would lead to an instability or collapse of lattice structure that seriously damages the long-term stability of Ir-based catalysts. This has been puzzling the development of advanced catalysts with high performance toward OER [60]. In our case, however, the as-synthesized $Sr_4Ir_3O_{10}$ displays a very good durability, even in acidic solution shown in Fig. 2f. It implies that the good structure stability can be attributed to an atomistic migration of the interstitial oxygen from the SrO rock-salt layer to the $SrIrO_3$ perovskite layer, followed by the moved interstitial oxygen supplemented by adsorbed oxygen from electrolyte. The total oxygen conversion from the adsorbed oxygen to interstitial oxygen and then lattice oxygen at atom level is illustrated in Fig. 5a. Based on the formation energies of different

oxygen species for the $Sr_4Ir_3O_{10}$ determined by DFT calculation shown in Fig. 5a, oxygen conversion from water to adsorbed oxygen to interstitial oxygen and finally lattice oxygen is an energy decline process. This further proves that the above three processes can occur spontaneously in thermodynamics. On the one hand, the SrO layer can grab water from electrolyte and then catalyze dissociation of the water into OH^- ions adsorbed at the surface during the OER. After that, the adsorbed OH^- ions can enter into tetrahedral interstices and then become interstitial oxygen of the SrO, especially under employed high potential (more than 1.2 V, around the OER potential of 1.23 V) condition that causes an electrochemical expansion of SrO layer, facilitating the transfer process form water to interstitial oxygens [20]. To explore the presence of interstitial oxygen, we conducted H_2 thermogravimetric tests on the fresh $Sr_4Ir_3O_{10}$ perovskite (Fig. 5b), and found that it is about 7.4% for interstitial oxygen content.

On the other hand, the interstitial oxygen in the SrO layer is structurally active and can further migrate to the lattice oxygen vacancies in the $SrIrO_3$ layer via a short-range interlayer diffusion, driven by an electrostatic attraction [17]. In this way, the lattice oxygen vacancies left by LOM process over the $SrIrO_3$ phase can be refilled by the interstitial oxygen migrated from the SrO monolayer, thus maintaining the structure stability of the $Sr_4Ir_3O_{10}$ during OER, as shown in Fig. 5a. To further verify the contribution of the mobile interstitial oxygen to stabilization, we put the synthesized catalyst in a hydrogen atmosphere at 600 °C for heat treatment for 0.5 h to fully remove the interstitial oxygen, and then carried out a control stability test. As expectedly, the treated sample exhibits a very poor stability (less than 0.5 h), compared with the pristine one (more than 35 h) shown in Fig. 5c. It proves the interstitial oxygen in SrO layer plays a key role in maintaining structure stability of the catalysts. Moreover, we detected the possible change in lattice oxygen vacancy using EPR tests and collected the oxygen vacancy intensity of the $Sr_4Ir_3O_{10}$ before and after OER. From the recorded EPR maps in Fig. 5d, the signal intensity of the lattice oxygen vacancy for the $Sr_4Ir_3O_{10}$ has almost no change, even after 35 h test. It is believed that the interstitial oxygen can move and refill into apical oxygen vacancies of IrO_6 octahedron [16]. This unique interlayer migration of interstitial oxygen from the SrO to $SrIrO_3$ layers can efficiently hinder the lattice damage or collapse caused by missing lattice oxygen , achieving an interstitial oxygen-stabilized LOM pathway, eventually ensuring the stability of the catalyst shown in Fig. 2f.

In this way, it achieves a closed-loop process of water splitting from electrolyte, interstitial oxygen, lattice oxygen to product oxygen molecule, as shown in Fig. 5e. During the OER, the SrO layer can absorb water from the electrolyte and then catalyze dissociation into OH^- ions, which are adsorbed at the surface. Following that, the adsorbed OH^- ions can enter tetrahedral interstices and become interstitial oxygen of the SrO, particularly when a high potential (more than 1.2 V, close to the OER potential of 1.23 V) is used, causing an electrochemical expansion of the SrO layer and facilitating the transfer process from water to interstitial oxygen [18]. It is thought that the interstitial oxygen can travel and replenish apical oxygen holes in the IrO_6 octahedron [20]. This unique interlayer migration of interstitial oxygen from the SrO to $SrIrO_3$ layers can efficiently prevent lattice damage or collapse caused by a lack of lattice oxygen, hence boosting stability. It is different from the sluggish AEM mechanism that only involves a conversion from adsorbed water to released O_2. Therefore, the interstitial oxygen assisted LOM mechanism, through a synergetic activation by interstitial and lattice oxygen together, should be responsible for the ultrahigh activity and stability of the synthesized $Sr_4Ir_3O_{10}$.

3.4. Active sites identified by proposed hybrid solvation model

For water splitting, water molecules are both reactant and solvent, so it is a key step that establishing a hybrid solvation model to accurately reveal the active sites of the $Sr_4Ir_3O_{10}$. Therefore, we established a hybrid solvation model to investigate the multiple identities of water for
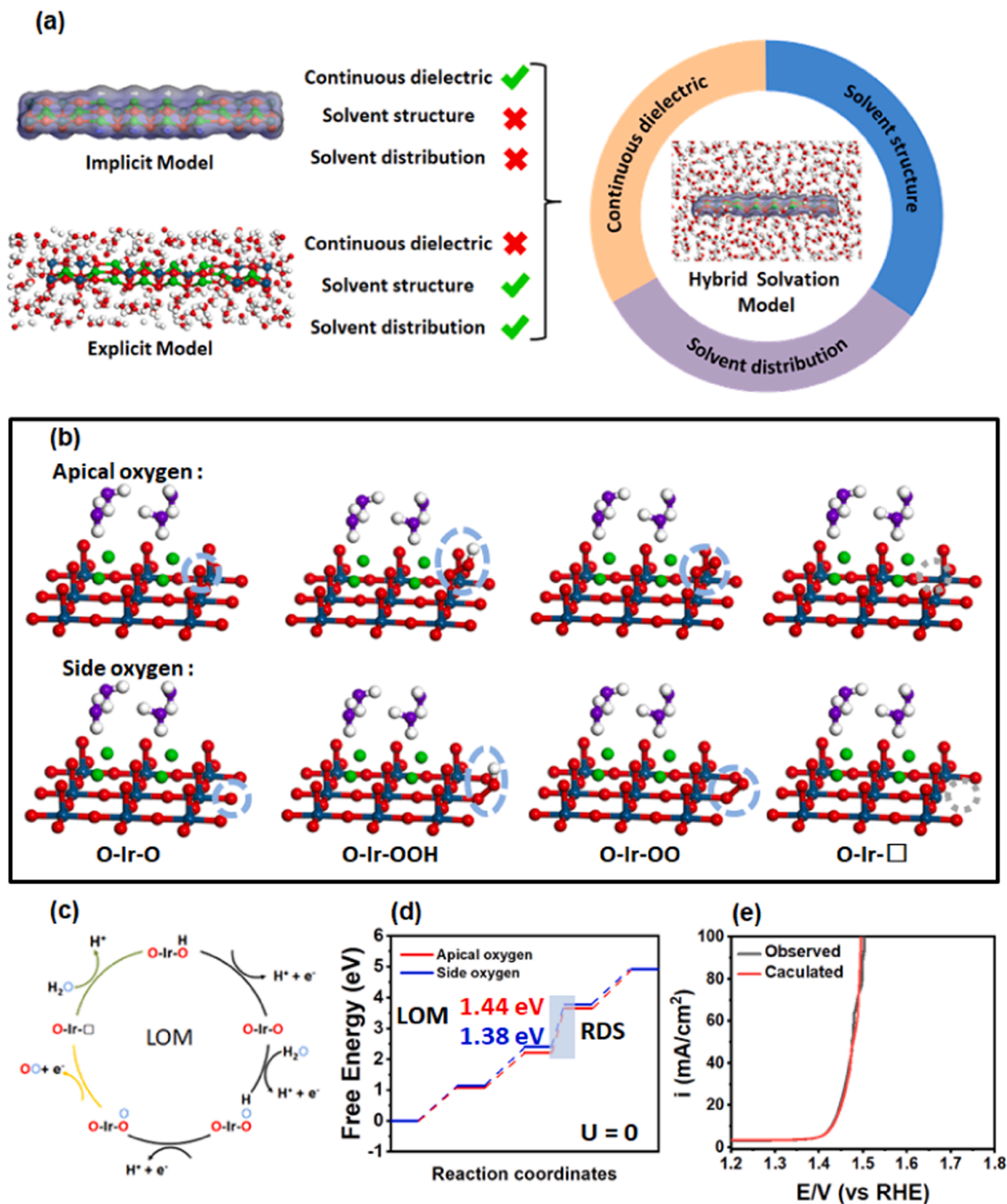
Fig. 6. (a) Schematic diagram of hybrid solvation model. (b) Adsorption kinetics with schematic illustration of the $Sr_4Ir_3O_{10}$ at different sites following LOM. Ir, Sr, O, and H are presented as blue, green, red, and white spheres, respectively. (c) OER via LOM process. (d) Free energy diagrams of the $Sr_4Ir_3O_{10}$ following LOM pathway with respect to reaction coordinates. (e) The calculated kinetic currents of OER on $Sr_4Ir_3O_{10}$.

OER in acidic environment, by combining an implicit solvation model for inert and continuous water that acts as conductive solvent (with certain dielectric constant) with an explicit solvation model for active water that participates in oxygen evolution shown in Fig. S24. The established hybrid solvation model can fully extract the role of water in OER, thus making the model more authentic and reliable, compared with either implicit or explicit solvation model [61,62]. As shown in Fig. 6a, the implicit solvation model can simulate the continuous dielectric action of solvent, while the explicit solvation model can simulate the influence of the structure and distribution of solvent molecules involved in the reaction. The hybrid solvation model can not only fully consider all the effects of solvents, but also solve the problems of incomplete filling and excessive calculation in the explicit solvation model [63]. According to the observation on the SrO-water interface by Halwidl [18], we built the explicitly solvated water molecules on the top of Sr atoms to obtain a solvation model close to the actual situation. And then, we calculated the water-surface interaction energy and inter-H_2O hydrogen bonding energy to confirm the reliability of the solvation model. As observed in Fig. S25, the water surface interaction energy is significantly larger than the inter-H_2O hydrogen bonding energy, proving that the active water molecules in the solvent model can act as a reactant during OER [32].

Based the established and optimized hybrid solvation model for the synthesized $Sr_4Ir_3O_{10}$ catalyst toward OER shown in Fig. S24, the obtained oxygen-involved intermediates produced by the stepwise OER kinetics via LOM pathway on the different active sites of the $Sr_4Ir_3O_{10}$ are shown in Fig. 6b. Herein, we considered two types of lattice oxygens (apical oxygen and side oxygen) acted as active sites in the $Sr_4Ir_3O_{10}$. For the apical oxygen, the water molecular from the solvent is firstly adsorbed by some lattice oxygen in the form of hydroxide, and then, after a process of removing H^+ from the adsorbed water, the generated dehydroxylation and the lattice oxygen chemically couple each other to form O_2 and leave some oxygen vacancies on the catalyst. For the side oxygen, the produced oxygen intermediates are almost similar to those of the apical oxygen but the coordination environments of the two lattice oxygens are different from each other shown in Fig. 6b. The side oxygen is inside the $SrIrO_3$ layer, which is different from the apical oxygen located at the junction of the SrO monolayer and $SrIrO_3$ layer. This difference may affect the catalytic activity. Based on the above stepwise adsorption processes, the identified and optimized OER kinetics via LOM over the $Sr_4Ir_3O_{10}$ are shown in Fig. 6c. As observed, the LOM is a typical process involved with decoupled proton–electron transfer, different from the AEM process on the catalyst shown in Fig. S26.

Moreover, we further analyze the free energy of the $Sr_4Ir_3O_{10}$ following LOM or AEM pathway with respect to reaction coordinates. For the LOM pathway on the $Sr_4Ir_3O_{10}$, the recorded onset potential of OER is 1.38 V (vs. RHE, same as below) for the side oxygen active site whereas it is 1.44 V for the apical oxygen active site. These LOM pathways are far lower than the onset potential of 1.94 V obtained by the AEM process shown in Fig. S27. It proves that the $Sr_4Ir_3O_{10}$ catalyst is more prone to occur the LOM process with lower energy barrier, compared with the AEM with higher energy barrier during the OER. It is believed that the LOM is faster in the reaction kinetics because it avoids a $OOH^* \rightarrow O_2$ process with high energy barrier existed in traditional AEM [64]. For the superior LOM, moreover, the side lattice oxygen site exhibits a lower onset potential and more uniform energy steps than the apical oxygen shown in Fig. 6d. In addition, Fig. 6e shows the recorded OER kinetic linear sweep voltammetry (LSV) curves by DFT calculation, based on the model structure of the side oxygen as the active sites. At 10 mA/cm^2, the calculated overpotential for OER over the catalyst is 205 mV, almost similar to that obtained by the experimental one. Even at higher currents (about 100 mA/cm^2), the calculated LSV curve match the experimental one very well, as evidenced by the results shown in Fig. 6e. Thus, it is concluded that the unique side lattice oxygen in the synthesized $Sr_4Ir_3O_{10}$ catalyst can act as the main active sites, which

should be responsible for the outstanding OER performance of the $Sr_4Ir_3O_{10}$ in acidic environment, based on the kinetic LSV simulation calculation results.

4. Conclusion

In summary, we fabricated a novel $Sr_4Ir_3O_{10}$ oxide with a layered structure composed by SrO rock-salt monolayer and $SrIrO_3$ perovskite multilayers, through a stepwise sol-gel strategy together with solid-phase sintering at high temperature. The layered oxide features delocalized interstitial oxygen in the SrO rock-salt phase and active lattice oxygen in the $SrIrO_3$ perovskite phase. In 0.1 M $HClO_4$, the catalyst exhibits a low overpotential of only 205 mV and an excellent long-term stability at 10 mA/cm^2, demonstrating the highest OER activity among metal oxides ever reported. The $Sr_4Ir_3O_{10}$ can even deliver a 50 h stability test operated at 10 mA/cm^2 in a PEMWE device. The high-performance can be attributed to a dynamic conversion process of oxygen species from adsorbed water to interstitial oxygen of SrO and then lattice oxygen of $SrIrO_3$, which enabling an interstitial oxygen assisted LOM process that has been proved by established hybrid solvation model for water splitting. Therefore, our proof-of-concept study not only creates an efficient and durable OER catalyst, but also opens up a new catalyst family for water splitting.

CRediT authorship contribution statement

The manuscript was written through the contributions of all authors. All authors have given approval to the final version of the manuscript.

Declaration of Competing Interest

The authors declare that they have no known competing financial interests or personal relationships that could have appeared to influence the work reported in this paper.

Data Availability

Data will be made available on request.

Appendix A. Supporting information

Supplementary data associated with this article can be found in the online version at doi:10.1016/j.apcatb.2023.123402.

References

[1] W. Jiang, Q. Ruan, J. Xie, X. Chen, Y. Zhu, J. Tang, Oxygen-doped carbon nitride aerogel: a self-supported photocatalyst for solar-to-chemical energy conversion, Appl. Catal. B-Environ. 236 (2018) 428–435, https://doi.org/10.1016/j.apcatb.2018.05.050.

[2] M. Kourtelesis, T.S. Moraes, L.V. Mattos, D.K. Niakolas, F.B. Noronha, X. Verykios, The effects of support morphology on the performance of Pt/CeO$_2$ catalysts for the low temperature steam reforming of ethanol, Appl. Catal. B-Environ. 284 (2021), 119757, https://doi.org/10.1016/j.apcatb.2020.119757.

[3] C. Li, R. Xu, S. Ma, Y. Xie, K. Qu, H. Bao, W. Cai, Z. Yang, Sulfur vacancies in ultrathin cobalt sulfide nanoflowers enable boosted electrocatalytic activity of nitrogen reduction reaction, Chem. Eng. J. 415 (2021), 129018, https://doi.org/10.1016/j.cej.2021.129018.

[4] J. Sun, P. Leng, Y. Xie, X. Yu, K. Qu, L. Feng, H. Bao, F. Luo, Z. Yang, Co single atoms and Co nanoparticle relay electrocatalyst for rechargeable zinc air batteries,

Appl. Catal. B-Environ. 319 (2022), 121905, https://doi.org/10.1016/j.apcatb.2022.121905.

[5] C. Chang, Y. Xie, F. Luo, S. Zhou, Z. Yang, Weakening s-d orbital hybridization of metallic iridium by tungsten atoms for acidic water splitting, Appl. Catal. A-Gen. 649 (2023), 118941, https://doi.org/10.1016/j.apcata.2022.118941.

[6] D.K. Liguras, D.I. Kondarides, X.E. Verykios, Production of hydrogen for fuel cells by steam reforming of ethanol over supported noble metal catalysts, Appl. Catal. B-Environ. 43 (2003) 345–354, https://doi.org/10.1016/S0926-3373(02)00327-2.

[7] K. Mori, K. Miyawaki, H. Yamashita, Ru and Ru–Ni nanoparticles on TiO2 support as extremely active catalysts for hydrogen production from ammonia–borane, ACS Catal. 6 (2016) 3128–3135, https://doi.org/10.1021/acscatal.6b00715.

[8] M. van der Spek, C. Banet, C. Bauer, P. Gabrielli, W. Goldthorpe, M. Mazzotti, S. T. Munkejord, N.A. Røkke, N. Shah, N. Sunny, D. Sutter, J.M. Trusler, M. Gazzani, Perspective on the hydrogen economy as a pathway to reach net-zero CO2 emissions in Europe, Energy Environ. Sci. 15 (2022) 1034–1077, https://doi.org/10.1039/D1EE02118D.

[9] S. Chatterjee, X. Peng, S. Intikhab, G. Zeng, N.N. Kariuki, D.J. Myers, N. Danilovic, J. Snyder, Nanoporous iridium nanosheets for polymer electrolyte membrane electrolysis, Adv. Energy Mater. 11 (2021), 2101438, https://doi.org/10.1002/aenm.202101438.

[10] C. Jiang, J. Yang, X. Han, H. Qi, H. Su, D. Zhao, L. Kang, X. Liu, J. Ye, J. Li, Z.-X. Guo, N. Kaltsoyannis, A. Wang, J. Tang, Crystallinity-modulated Co2−xVxO4 nanoplates for efficient electrochemical water oxidation, ACS Catal. 11 (2021) 14884–14891, https://doi.org/10.1021/acscatal.1c04618.

[11] M. Thangamuthu, K. Vankayala, L. Xiong, S. Conroy, X. Zhang, J. Tang, Tungsten oxide-based Z-scheme for visible light-driven hydrogen production from water splitting, ACS Catal. 13 (2023) 9113–9124, https://doi.org/10.1021/acscatal.3c01312.

[12] J. Zhang, Y. Ye, Z. Wang, Y. Xu, L. Gui, B. He, L. Zhao, Probing dynamic self-reconstruction on perovskite fluorides toward ultrafast oxygen evolution, Adv. Sci. 9 (2022), 2201916, https://doi.org/10.1002/advs.202201916.

[13] M. You, L. Gui, X. Ma, Z. Wang, Y. Xu, J. Zhang, J. Sun, B. He, L. Zhao, Electronic tuning of SrIrO3 perovskite nanosheets by sulfur incorporation to induce highly efficient and long-lasting oxygen evolution in acidic media, Appl. Catal. B-Environ. 298 (2021), 120562, https://doi.org/10.1016/j.apcatb.2021.120562.

[14] X. Xu, Y. Pan, Y. Zhong, R. Ran, Z. Shao, Ruddlesden–Popper perovskites in electrocatalysis, Mater. Horiz. 7 (2020) 2519–2565, https://doi.org/10.1039/D0MH00477D.

[15] J.D. Jorgensen, B. Dabrowski, S. Pei, D.R. Richards, D.G. Hinks, Structure of the interstitial oxygen defect in La2NiO4+δ, Phys. Rev. B 40 (1989) 2187–2199, https://doi.org/10.1103/PhysRevB.40.2187.

[16] C. Zhu, H. Tian, B. Huang, G. Cai, C. Yuan, Y. Zhang, Y. Li, G. Li, H. Xu, M.-R. Li, Boosting oxygen evolution reaction by enhanced intrinsic activity in Ruddlesden−Popper iridate oxides, Chem. Eng. J. 423 (2021), 130185, https://doi.org/10.1016/j.cej.2021.130185.

[17] A. Chroneos, D. Parfitt, J.A. Kilner, R.W. Grimes, Anisotropic oxygen diffusion in tetragonal La2NiO4+δ: molecular dynamics calculations, J. Mater. Chem. A 20 (2010) 266–270, https://doi.org/10.1039/B917118E.

[18] D. Halwidl, B. Stöger, W. Mayr-Schmölzer, J. Pavelec, D. Fobes, J. Peng, Z. Mao, G. S. Parkinson, M. Schmid, F. Mittendorfer, J. Redinger, U. Diebold, Adsorption of water at the SrO surface of ruthenates, Nat. Mater. 15 (2016) 450–455, https://doi.org/10.1038/nmat4512.

[19] E. Magnone, G. Cerisola, M. Ferretti, A. Barbucci, Electrochemical investigation of oxygen intercalation into La2CuO4+δ phases, J. Solid State Chem. 144 (1999) 8–15, https://doi.org/10.1006/jssc.1998.7970.

[20] A.W.H. Whittingham, R.D.L. Smith, Electrochemically induced phase changes in La2CuO4 during cathodic electrocatalysis, ChemElectroChem 6 (2019) 5116–5123, https://doi.org/10.1002/celc.201901412.

[21] A. Grimaud, O. Diaz-Morales, B. Han, W.T. Hong, Y.-L. Lee, L. Giordano, K. A. Stoerzinger, M.T.M. Koper, Y. Shao-Horn, Activating lattice oxygen redox reactions in metal oxides to catalyse oxygen evolution, Nat. Chem. 9 (2017) 457–465, https://doi.org/10.1038/nchem.2695.

[22] B. Han, A. Grimaud, L. Giordano, W.T. Hong, O. Diaz-Morales, L. Yueh-Lin, J. Hwang, N. Charles, K.A. Stoerzinger, W. Yang, M.T.M. Koper, Y. Shao-Horn, Iron-based perovskites for catalyzing oxygen evolution reaction, J. Phys. Chem. C 122 (2018) 8445–8454, https://doi.org/10.1021/acs.jpcc.8b01397.

[23] H. Liu, X. Li, C. Peng, L. Zhu, Y. Zhang, H. Cheng, J. Cui, Q. Wu, Y. Zhang, Z. Chen, W. Zou, W. Gu, H. Huang, J. Wang, B. Ye, Z. Fu, Y. Lu, Activating the lattice oxygen in (Bi0.5Co0.5)2O3 by vacancy modulation for efficient electrochemical water oxidation, J. Mater. Chem. A 8 (2020) 13150–13159, https://doi.org/10.1039/D0TA03411H.

[24] S.B. Scott, J. Kibsgaard, P.C.K. Vesborg, I. Chorkendorff, Tracking oxygen atoms in electrochemical CO oxidation - Part II: Lattice oxygen reactivity in oxides of Pt and Ir, Electrochim. Acta 374 (2021), 137844, https://doi.org/10.1016/j.electacta.2021.137844.

[25] Y. Wu, Y. Zhao, P. Zhai, C. Wang, J. Gao, L. Sun, J. Hou, Triggering lattice oxygen activation of single-atomic mo sites anchored on Ni–Fe oxyhydroxides nanoarrays for electrochemical water oxidation, Adv. Mater. 34 (2022), 2202523, https://doi.org/10.1002/adma.202202523.

[26] J.S. Yoo, X. Rong, Y. Liu, A.M. Kolpak, Role of lattice oxygen participation in understanding trends in the oxygen evolution reaction on perovskites, ACS Catal. 8 (2018) 4628–4636, https://doi.org/10.1021/acscatal.8b00612.

[27] T. Xia, C. Liu, Y. Lu, W. Jiang, H. Li, Y. Ma, Y. Wu, G. Che, Regulating Ru-based double perovskite against lattice oxygen oxidation by incorporating Ir for efficient and stable acidic oxygen evolution reaction, Appl. Surf. Sci. 605 (2022) 154727, https://doi.org/10.1016/j.apsusc.2022.154727.

[28] D. Lee, H.N. Lee, Controlling oxygen mobility in ruddlesden–popper oxides, Materials 10 (2017) 368, https://doi.org/10.3390/ma10040368.

[29] J.P. Perdew, K. Burke, M. Ernzerhof, Generalized gradient approximation made simple, Phys. Rev. Lett. 77 (1996) 3865–3868, https://doi.org/10.1103/PhysRevLett.77.3865.

[30] A.A. Peterson, F. Abild-Pedersen, F. Studt, J. Rossmeisl, J.K. Nørskov, How copper catalyzes the electroreduction of carbon dioxide into hydrocarbon fuels, Energy Environ. Sci. 3 (2010) 1311–1315, https://doi.org/10.1039/C0EE00071J.

[31] Y. Ying, K. Fan, X. Luo, J. Qiao, H. Huang, Unravelling the origin of bifunctional OER/ORR activity for single-atom catalysts supported on C2N by DFT and machine learning, J. Mater. Chem. A 9 (2021) 16860–16867, https://doi.org/10.1039/D1TA04256D.

[32] A.S. Nair, B. Pathak, Accounting for dispersion effects in the DFT framework of electrocatalysis: a hybrid solvation model-based case study of the oxygen reduction reaction, J. Phys. Chem. C 126 (2022) 6171–6188, https://doi.org/10.1021/acs.jpcc.1c09207.

[33] K. Dong, J. Hou, L. Miao, Z. Jin, D. Wang, Y. Teng, W. Liu, A comparative study of the R-P phase Srn+1FenO3n+1 (n= 1, 2 and 3) cathodes for intermediate temperature solid oxide fuel cells, Ceram. Int. 46 (2020) 19335–19342, https://doi.org/10.1016/j.ceramint.2020.04.274.

[34] Y. Zhu, H.A. Tahini, Z. Hu, Z.-G. Chen, W. Zhou, A.C. Komarek, Q. Lin, H.-J. Lin, C.-T. Chen, Y. Zhong, M.T. Fernández-Díaz, S.C. Smith, H. Wang, M. Liu, Z. Shao, Boosting oxygen evolution reaction by creating both metal ion and lattice-oxygen active sites in a complex oxide, Adv. Mater. 32 (2020), 1905025, https://doi.org/10.1002/adma.201905025.

[35] C. Cao, C. Shang, X. Li, Y. Wang, C. Liu, X. Wang, S. Zhou, J. Zeng, Dimensionality control of electrocatalytic activity in perovskite nickelates, Nano Lett. 20 (2022，) 2837–2842, https://doi.org/10.1021/acs.nanolett.0c00553.

[36] H. Wang, D. Lu, W. Wang, Y. Ding, Y. Ji, X. Shen, Y. Yao, Y. Long, R. Yu, Tetragonal and orthorhombic phases in polycrystalline Sr4Ir3O10 synthesized by high-pressure and high-temperature technique, Phys. Status Solidi B 260 (2023) 2300050, https://doi.org/10.1002/pssb.202300050.

[37] T. Nakamura, R. Oike, Y. Ling, Y. Tamenori, K. Amezawa, The determining factor for interstitial oxygen formation in Ruddlesden–Popper type La2NiO4-based oxides, Phys. Chem. Chem. Phys. 18 (2016) 1564–1569, https://doi.org/10.1039/C5CP05993C.

[38] X. Wang, H. Zhong, S. Xi, W.S.V. Lee, J. Xue, Understanding of oxygen redox in the oxygen evolution reaction, Adv. Mater. 34 (2022) 2107956, https://doi.org/10.1002/adma.202107956.

[39] J. Shan, T. Ling, K. Davey, Y. Zheng, S.-Z. Qiao, Transition-metal-doped ruir bifunctional nanocrystals for overall water splitting in acidic environments, Adv. Mater. 31 (2019), 1900510, https://doi.org/10.1002/adma.201900510.

[40] B. Jiang, Y. Guo, J. Kim, A.E. Whitten, K. Wood, K. Kani, A.E. Rowan, J. Henzie, Y. Yamauchi, Mesoporous metallic iridium nanosheets, J. Am. Chem. Soc. 140 (2018) 12434–12441, https://doi.org/10.1021/jacs.8b05206.

[41] L. Yang, G. Yu, X. Ai, W. Yan, H. Duan, W. Chen, X. Li, T. Wang, C. Zhang, X. Huang, J.-S. Chen, X. Zou, Efficient oxygen evolution electrocatalysis in acid by a perovskite with face-sharing IrO6 octahedral dimers, Nat. Commun. 9 (2018), 5236, https://doi.org/10.1038/s41467-018-07678-w.

[42] W. Gou, M. Zhang, Y. Zou, X. Zhou, Y. Qu, Iridium-chromium oxide nanowires as highly performed OER catalysts in acidic media, ChemCatChem 11 (2019) 6008–6014, https://doi.org/10.1002/cctc.201901411.

[43] L.C. Seitz, C.F. Dickens, K. Nishio, Y. Hikita, J. Montoya, A. Doyle, C. Kirk, A. Vojvodic, H.Y. Hwang, J.K. Norskov, T.F. Jaramillo, A highly active and stable IrOx/SrIrO3 catalyst for the oxygen evolution reaction, Science 353 (2016) 1011–1014, https://doi.org/10.1126/science.aaf5050.

[44] Y. Pi, Q. Shao, P. Wang, J. Guo, X. Huang, General formation of monodisperse IrM (M = Ni, Co, Fe) bimetallic nanoclusters as bifunctional electrocatalysts for acidic overall water splitting, Adv. Funct. Mater. 27 (2017), 1700886, https://doi.org/10.1002/adfm.201700886.

[45] W.Q. Zaman, W. Sun, M. Tariq, Z. Zhou, U. Farooq, Z. Abbas, L. Cao, J. Yang, Iridium substitution in nickel cobaltite renders high mass specific OER activity and durability in acidic media, Appl. Catal. B-Environ. 244 (2019) 295–302, https://doi.org/10.1016/j.apcatb.2018.10.041.

[46] L. Fu, X. Zeng, G. Cheng, W. Luo, IrCo nanodendrite as an efficient bifunctional electrocatalyst for overall water splitting under acidic conditions, ACS Appl. Mater. Interfaces 10 (2018) 24993–24998, https://doi.org/10.1021/acsami.8b08717.

[47] J. Zhang, G. Wang, Z. Liao, P. Zhang, F. Wang, X. Zhuang, E. Zschech, X. Feng, Iridium nanoparticles anchored on 3D graphite foam as a bifunctional electrocatalyst for excellent overall water splitting in acidic solution, Nano Energy 40 (2017) 27–33, https://doi.org/10.1016/j.nanoen.2017.07.054.

[48] J. Guan, D. Li, R. Si, S. Miao, F. Zhang, C. Li, Synthesis and demonstration of subnanometric iridium oxide as highly efficient and robust water oxidation catalyst, ACS Catal. 7 (2017) 5983–5986, https://doi.org/10.1021/acscatal.7b02082.

[49] K. Kadakia, M.K. Datta, O.I. Velikokhatnyi, P.H. Jampani, P.N. Kumta, Fluorine doped (Ir,Sn,Nb)O2 anode electro-catalyst for oxygen evolution via PEM based water electrolysis, Int. J. Hydrog. Energy 39 (2014) 664–674, https://doi.org/10.1016/j.ijhydene.2013.10.123.

[50] S. Ge, R. Xie, B. Huang, Z. Zhang, H. Liu, X. Kang, S. Hu, S. Li, Y. Luo, Q. Yu, J. Wang, G. Chai, L. Guan, H.-M. Cheng, B. Liu, A robust chromium–iridium oxide catalyst for high-current–density acidic oxygen evolution in proton exchange membrane electrolyzers, Energy Environ. Sci. (2023), https://doi.org/10.1039/D3EE01192E.

[51] T.B.N. Huynh, J. Song, H.E. Bae, Y. Kim, M.D. Dickey, Y.-E. Sung, M.J. Kim, O. J. Kwon, Ir–Ru electrocatalysts embedded in N-doped carbon matrix for proton

exchange membrane water electrolysis (n/a), Adv. Funct. Mater. (2023), 2301999, https://doi.org/10.1002/adfm.202301999.

[52] Y. Liu, T.G. Kelly, J.G. Chen, W.E. Mustain, Metal carbides as alternative electrocatalyst supports, ACS Catal. 3 (2013) 1184–1194, https://doi.org/10.1021/cs4001249.

[53] M.T.M. Koper, Theory of multiple proton–electron transfer reactions and its implications for electrocatalysis, Chem. Sci. 4 (2013) 2710–2723, https://doi.org/10.1039/C3SC50205H.

[54] L. Giordano, B. Han, M. Risch, W.T. Hong, R.R. Rao, K.A. Stoerzinger, Y. Shao-Horn, pH dependence of OER activity of oxides: current and future perspectives, Catal. Today 262 (2016) 2–10, https://doi.org/10.1016/j.cattod.2015.10.006.

[55] J.T. Mefford, X. Rong, A.M. Abakumov, W.G. Hardin, S. Dai, A.M. Kolpak, K. P. Johnston, K.J. Stevenson, Water electrolysis on $La_{1-x}Sr_xCoO_{3-\delta}$ perovskite electrocatalysts, Nat. Commun. 7 (2016), 11053, https://doi.org/10.1038/ncomms11053.

[56] C. Shang, C. Cao, D. Yu, Y. Yan, Y. Lin, H. Li, T. Zheng, X. Yan, W. Yu, S. Zhou, J. Zeng, Electron correlations engineer catalytic activity of pyrochlore iridates for acidic water oxidation, Adv. Mater. 31 (2019), 1805104, https://doi.org/10.1002/adma.201805104.

[57] N. Zhang, X. Feng, D. Rao, X. Deng, L. Cai, B. Qiu, R. Long, Y. Xiong, Y. Lu, Y. Chai, Lattice oxygen activation enabled by high-valence metal sites for enhanced water oxidation, Nat. Commun. 11 (2020), 4066, https://doi.org/10.1038/s41467-020-17934-7.

[58] H. Sun, X. Xu, Y. Song, W. Zhou, Z. Shao, Designing high-valence metal sites for electrochemical water splitting, Adv. Funct. Mater. 31 (2021), 2009779, https://doi.org/10.1002/adfm.202009779.

[59] W. Zhao, J. Qin, W. Teng, J. Mu, C. Chen, J. Ke, J.C. Huang, B. Liu, S. Wang, Catalytic photo-redox of simulated air into ammonia over bimetallic MOFs nanosheets with oxygen vacancies, Appl. Catal. B-Environ. 305 (2022), 121046, https://doi.org/10.1016/j.apcatb.2021.121046.

[60] N. Zhang, Y. Chai, Lattice oxygen redox chemistry in solid-state electrocatalysts for water oxidation, Energy Environ. Sci. 14 (2021) 4647–4671, https://doi.org/10.1039/D1EE01277K.

[61] H. Lee, H.-K. Lim, H. Kim, Hydration thermodynamics of non-polar aromatic hydrocarbons: comparison of implicit and explicit solvation models, Molecules 23 (2018) 2927, https://doi.org/10.3390/molecules23112927.

[62] S.N. Steinmann, P. Sautet, C. Michel, Solvation free energies for periodic surfaces: comparison of implicit and explicit solvation models, Phys. Chem. Chem. Phys. 18 (2016) 31850–31861, https://doi.org/10.1039/C6CP04094B.

[63] M. Gupta, E.F. da Silva, H.F. Svendsen, Postcombustion CO_2 capture solvent characterization employing the explicit solvation shell model and continuum solvation models, J. Phys. Chem. B 120 (2016) 9034–9050, https://doi.org/10.1021/acs.jpcb.6b04049.

[64] J. Song, C. Wei, Z.-F. Huang, C. Liu, L. Zeng, X. Wang, Z.J. Xu, A review on fundamentals for designing oxygen evolution electrocatalysts, Chem. Soc. Rev. 49 (2020) 2196–2214, https://doi.org/10.1039/C9CS00607A.